Supporting Information

Rational design and kinetics study of flexible sodium-ion full batteries based on binder-free composite film electrodes

Keliang Zhang,[a] Xudong Zhang,*[a] Wen He,*[a] Wangning Xu,[a] Guogang Xu,[b] Xinli Yi,[d] Xuena Yang[a] and Jiefang Zhu*[c]

[a]College of Material Science and Engineering, Qilu University of Technology (Shandong Academy of Sciences), Jinan 250353, China.
[b]College of Material Science and Engineering, Shandong University of Science and Technology, Qingdao 266590, China.
[c]Department of Chemistry-Ångström Laboratory, Uppsala University, Box 538, SE-75121 Uppsala, Sweden.

Sections:

S1. The contrast of constitute and electrochemical performances of flexible full batteries

Table S1 Constitute and electrochemical performances of flexible full batteries

Flexible full batteries	Flexible cathode material	Flexible anode material	Rate performance (mAh g^{-1})	Cyclic stability (mAh g^{-1})	Ref
Flexible sodium ion full battery (FSIFB)	**BFCF-NVP/hard carbon fiber (HCF)**	**PGN/SiC/HCF**	**51.7 at 15 A g^{-1}**	**30 after 1000 cycles** at 5 A g^{-1}	**Our work**
FSIFB	NVP@C/ reduced graphene oxide (rGO)	NVP@C /rGO	74.1 at 0.5 C	47.8 after 200 cycles at 3 C	[1]
FSIFB	NVP/carbon cloth (CC)	TiO_2/ CC			[2]
FSIFB	NVP/rGO	Sb/rGO		400 after 100 cycles at 100 mA g^{-1}	[3]
FSIFB	NVP@mp-CNSs /carbon fiber cloth (CFC)	VO_2@mp-CNSs /CFC	85 at 0.1 A g^{-1}	40 after 2000 cycles at 1 A g^{-1}	[4]
Flexible lithium ion full battery (FLIFB)	LFP/ graphene foam (GF)	LTO/GF	117 at 10 C	4% capacity loss after100 cycles at 10 C	[5]
FLIFB	LFPO nanosheet/Al foils	2D ZMO–G/Cu foils	90 at 2 C	No obvious capacity decay at 10 C after 100 cycles,	[6]
FLIFB	LMO/stainless steel cloth (SSC)	LTO/SSC	168 at 2 C	163 after 100 cycles at 2C	[7]
Flexible Li/Na-ion full cell	PTCDA/CNT/rGO	Sodiated electrospun carbon nanofiber	35 at 2 A g^{-1}	78.0 after 200 cycles at 0.2 A g^{-1}	[8]

S2. The contrast of energy density of sodium ion batteries and the current rates of the BFCF-NVP/HCF cathode for FSIFB

Table S2 Contrast of energy density of different sodium ion batteries

Sodium ion batteries	Cathode material	Anode material	Specific energy density (Wh kg^{-1})	Current rate	Ref
Flexible sodium ion full battery (FSIFB)	**BFCF-NVP/hard carbon fiber (HCF)**	**PGN/SiC/HCF**	**234.1**	**0.5 A g^{-1}**	**Our work**
Sodium ion full battey	$Na_3V_2(PO_4)_3$ (NVP)	Hard carbon (HC)	258	0.2 C	[9]
Sodium ion full battey	$Na_{0.67}Ni_{0.41}Mn_{0.72}O_2$ (NNMO)	SnSe NSCs	141	30 μA	[10]
Dual-ion battery	Tin-Graphite	Sn foil	144	150 mA g^{-1}	[11]
Sodium ion full battey	C-NVPF	CHCS-CuP2	180	80 mA g^{-1}	[12]
Sodium ion battey	$Na[Li_{0.05}Mn_{0.50}Ni_{0.30}Cu_{0.10}Mg_{0.05}]O_2$	Sodium metal	215	0.1 C	[13]
Sodium ion hybrid capacitor	CMT	SnS/aCMT	115	0.5–4.0 V	[14]
Sodium ion full battey	$Na_3V_2(PO_4)_3$/C	Bi@N–C	119	50 mA g–1	[15]

Table S3 Details of the current rates of the BFCF-NVP/HCF cathode for FSIFB**s**

Total loading weight (mg)	Actual mass loading (mg cm^{-2})	Area (cm^2)	Current (mA)	Current rate (A g^{-1})
4.5	2.34	1	0.025	About 0.01*
4.5	2.34	1	0.125	0.05
4.5	2.34	1	0.650	0.25
4.5	2.34	1	1.25	0.5
4.5	2.34	1	2.5	1
4.5	2.34	1	5	2
4.5	2.34	1	12.5	5
4.5	2.34	1	37.5	15
4.5	2.34	1	50	20

*The calculation process is as follows: the actual mass loading of NVP active material is 2.34 mg cm^{-2}; the area of filter paper is 1*1=1.0 cm^2. So the actual current rate is 0.025 (current)/2.34 (mass loading)/1(area)=10.6 mA g^{-1} =0.01A g^{-1}.

S3. Preparation process for GN/SiC/HCF and PGN/SiC/HCF anodes

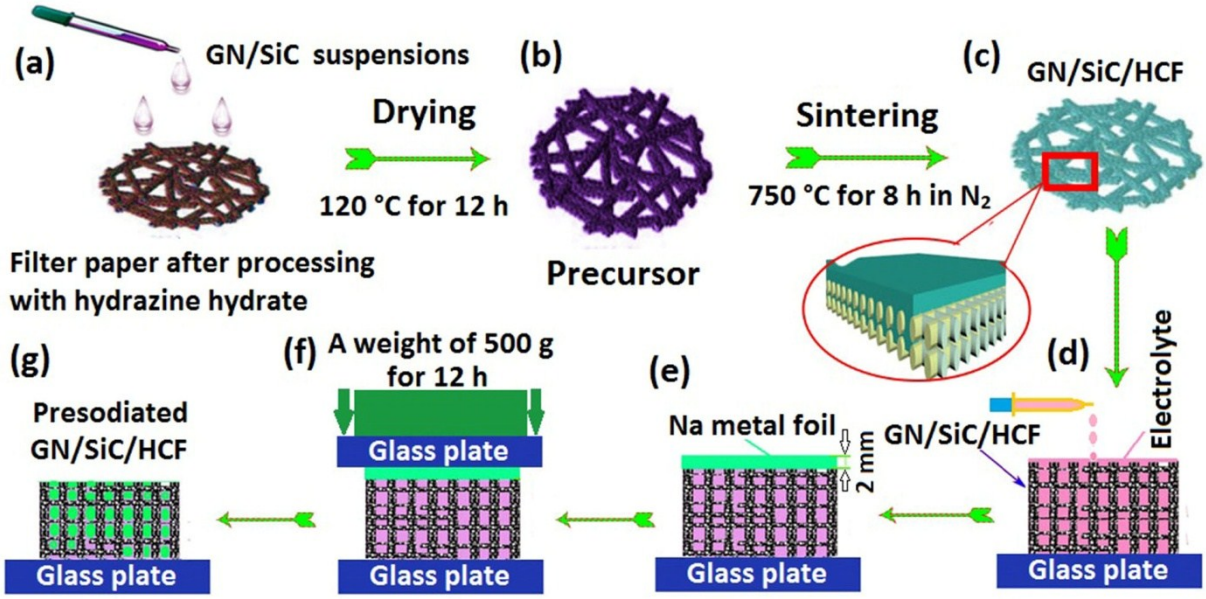

Fig. S1 Schematic illustration of the preparation process for GN/SiC/HCF and PN/SiC/HCF anodes.

S4. Materials characterization

X-ray diffraction (XRD) measurement employing with Cu-Kα radiation (LabX XRD-6100; Shimadzu) was performed with Cu-Kα radiation using LabX XRD-6100; Shimadzu. Field-emission scanning electron microscopy (SEM) images were taken by a Quanta 200 scanning electron microscope equipped with an X-ray energy dispersive spectrometer (EDS) operating at 20 kV. Transmission electron microscopy (TEM) images were taken by a Philips Tecnai 20U-TWIN microscope operating at 300 kV. The pore size distribution and nitrogen adsorption-destribution isotherms were measured at 77 K on a computer controlled sorption analyzer. Raman spectroscopic analysis was carried out using a RenishawIn-Via Raman microscopic instrument.

S5. Videos of the assembly process and potential application for FSIFBs (Videos1-2)

S6. Flexibility test of the pouch-type FSIFBs

Fig. S2 Photographs of the pouch-type FSIFB assembled with the BFCF-NVP/HCF cathode and the PGN/SiC/HCF anode, showing different luminosity of lighted LED bulb driven by the FSIFB after different bending cycles in a bending angle of 30–90°.

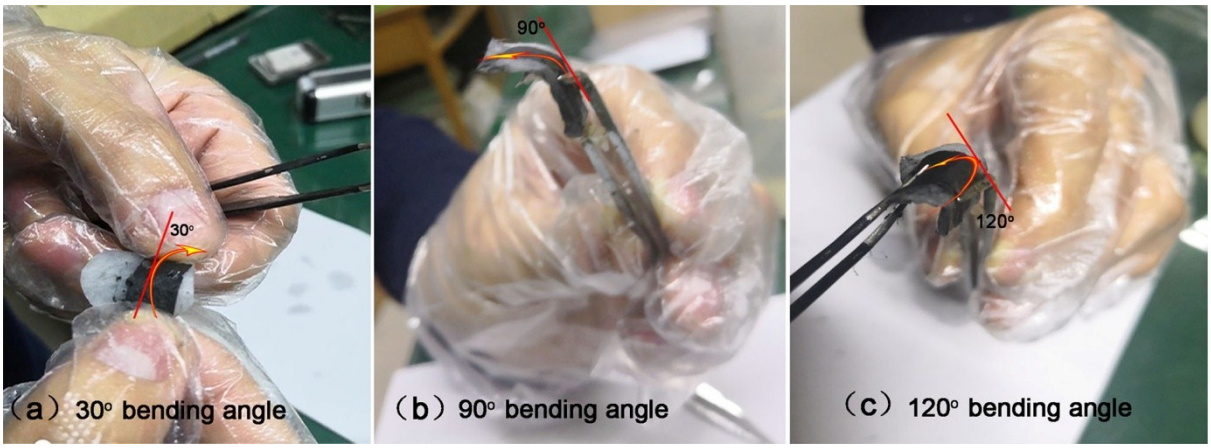

Fig. S3 Photographs of the BFCF-NVP/HCF cathode at different bending angles from the pouch-type FSIFB disassembled after 1600 bending cycles.

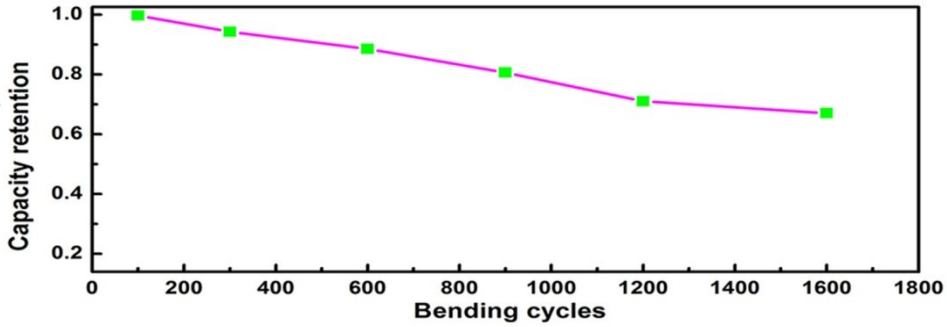

Fig. S4 Capacity retention of this FSIFB assembled with the BFCF-NVP/HCF cathode and the PGN/SiC/HCF anode at 0.5 **A g^{-1}** before and after different bending cycles in a bending angle of 30–90°.

Table S4 R_{SEI}, R_{ct}, and D_{Na} in Figure 4d.

Cycle number	R_{SEI} (Ω)	R_{CT} (Ω)	$D_{Na}\times10^{-13}$
2nd	83.8	93.1	39.70
12th	85.2	131.8	82.59
27th	86.4	219.2	123.52
36th	86.6	242.5	127.00

S7. Electrochemical performances of the different cathodes in SIHCs

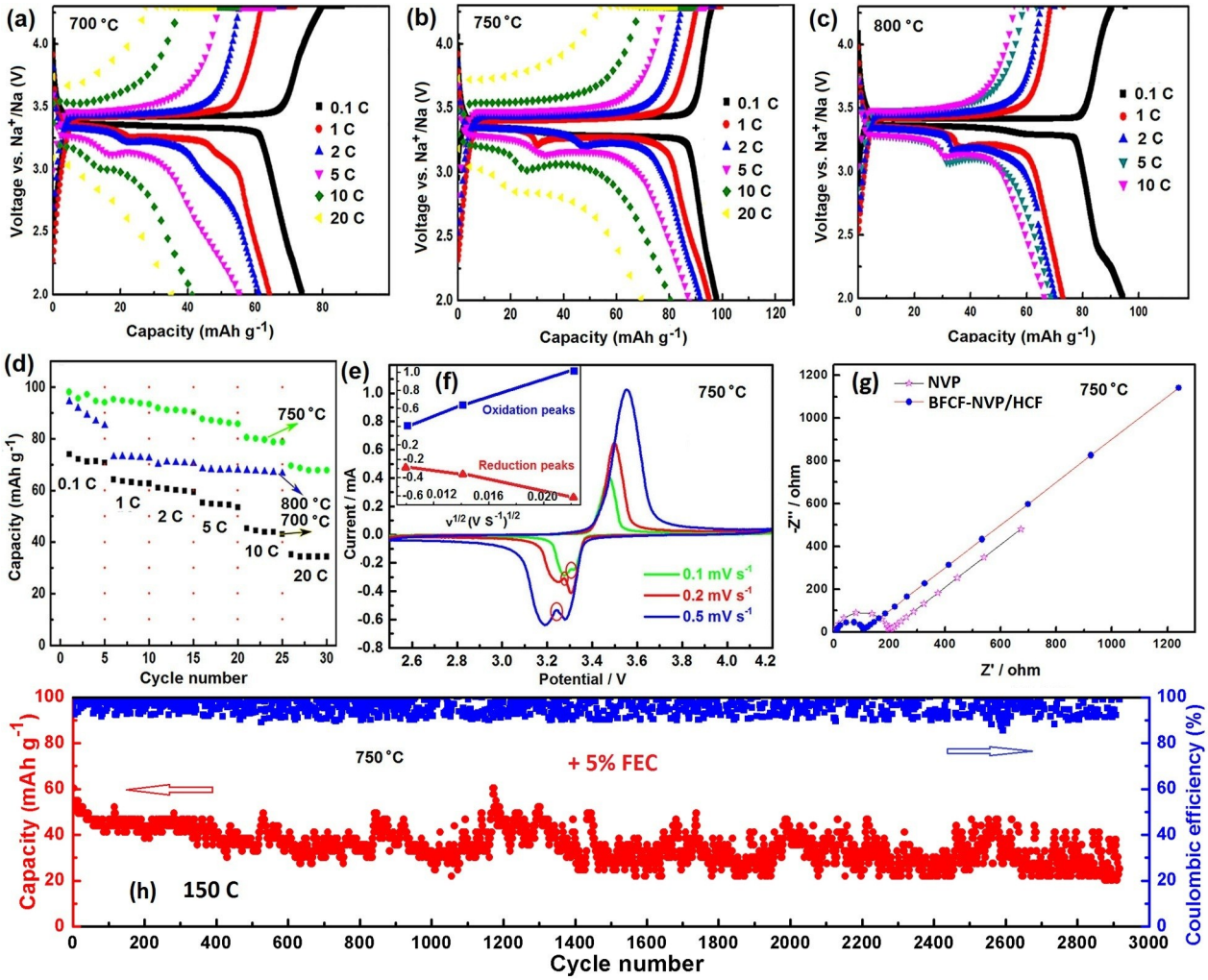

Fig. S5 Electrochemical performances of the different BFCF-NVP/HCF cathodes in the sodium ion half-cell (SIHC) form and using 1 M $NaClO_4$ electrolyte (EC: PC (1:1, v/v) + 0% FEC). (a-c) Charge–discharge curves of the cathodes synthesized at different tempratures. (d) Rate capability of the cathodes synthesized at differing temperatures. (e) CV curves and of the BFCF-NVP/HCF cathode synthesized at 750 °C. (f) The corresponding relationship between the squareroot of the scan rate, $v^{1/2}$, and peak current, ip. (g) EIS curves of the BFCF-NVP/HCF and blank NVP cathode synthesized at 750 °C. (h) The cycling performance of the BFCF-NVP/HCF cathode with coulombic efficiency over 2905 cycles in 1 M $NaClO_4$ electrolyte (EC: PC (1:1, v/v) + 5% FEC) at a 150 C rate.

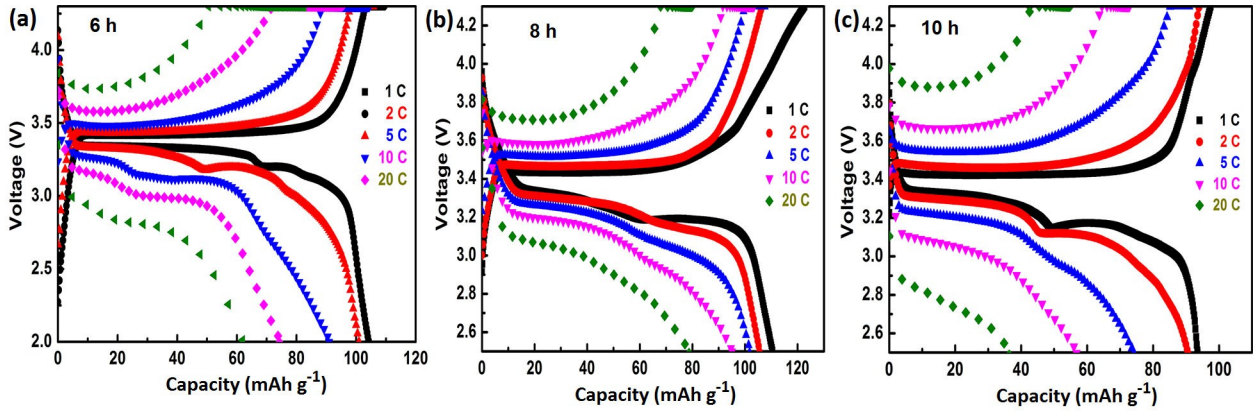

Fig. S6 Charge–discharge curves of the BFCF-NVP/HCF cathodes synthesized with different sintered time at 750 °C, (a) 6 h, (b) 8 h, (c) 10 h.

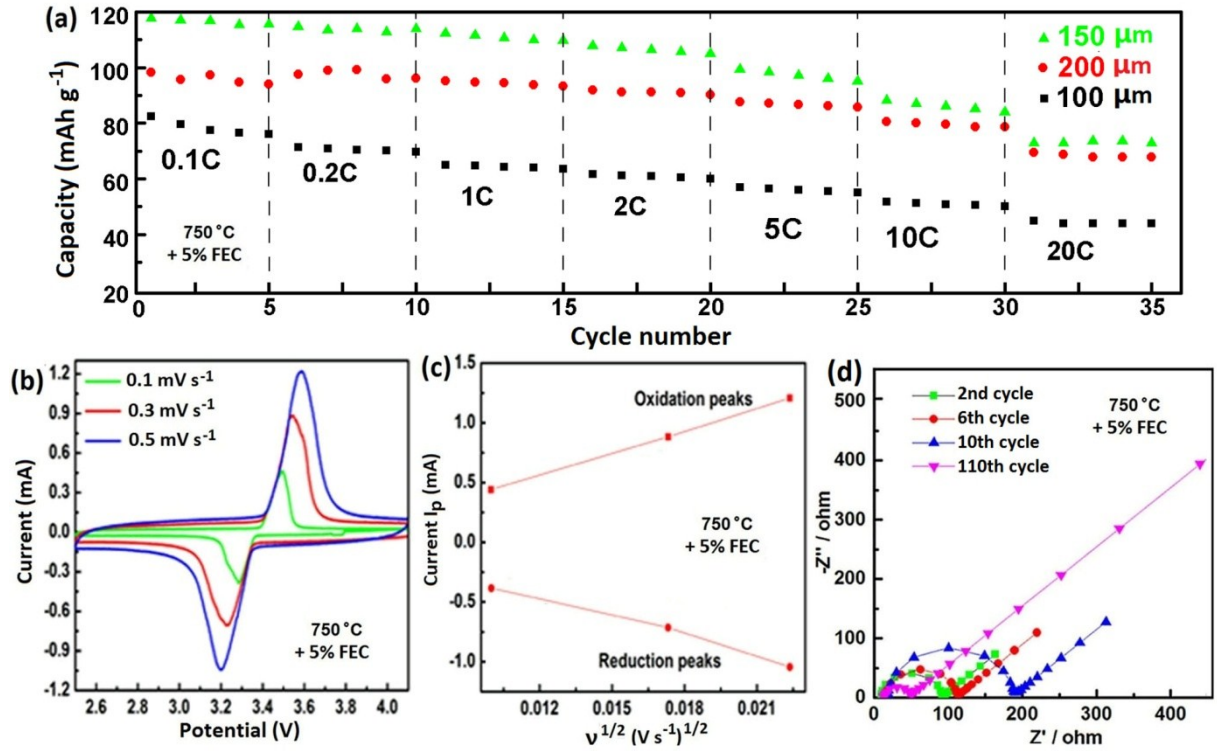

Fig. S7 Electrochemical performances of the BFCF-NVP/HCF cathodes synthesized at 750 °C in the sodium ion half-cell (SIHC) format and 1 M $NaClO_4$ electrolyte (EC: PC (1:1, v/v) + 5% FEC). (a) Rate capability of BFCF-NVP/HCF cathodes with the different thickness. (b) CV curve profiles of BFCF-NVP/HCF cathode with the thickness of 150 μm at different scan rates. (c) The corresponding relationship between the square root of the scan rate, $v^{1/2}$, and peak current, Ip at a scan rate of 0.3 mV s^{-1}. (d) EIS curves of BFCF-NVP/HCF cathode with the thickness of 150 μm in different cycles.

The cyclic voltammogram (CV) and electrochemical impedance spectroscopy (EIS) performances of the BFCF-NVP/HCF cathode synthesized at 750 °C were measured in the SIHC format, which can help to clarify the ohmic resistance, polarization resistance and the reasons of capacity loss. Fig. S7b shows the CV

curves of BFCF-NVP/HCF cathode synthesized at 750 °C at different scan rates using 1 M $NaClO_4$ electrolyte (EC: PC (1:1, v/v) + 5% FEC) in the SIHC form vs. Na^+/Na. The obvious redox peaks are assigned to the extraction/insertion of two Na ions during the two compositional transitions between $Na_3V_2(PO_4)_3$ and $NaV_2(PO_4)_3$. With the increase of scanning rate, the cathodic and anodic peaks shift to left and right, respectively, and the peak intensity increased. Fig. S7c shows the linear relationship between the peak current I_p and the square root of the scan rate $v^{1/2}$, confirming its diffusion controlled behaviour. Fig. S7d shows the internal resistance changes of the BFCF-NVP/HCF cathode in the 5% FEC electrolyte after different cycles. The R_{ct} after 2 cycles was 46.33 Ω, and then increased to 57.25, 95.01 Ω after 6, 10 cycles, respectively. Finally, it decreased to 25.57 Ω after 110 cycles. The increase of R_{ct} in the first 10 cyclesis is mainly ascribed to the progressive growth of solid electrolyteinterface (SEI), then decreased after 110 cycles. [16-18]

S8. Characterizations of the different anodes

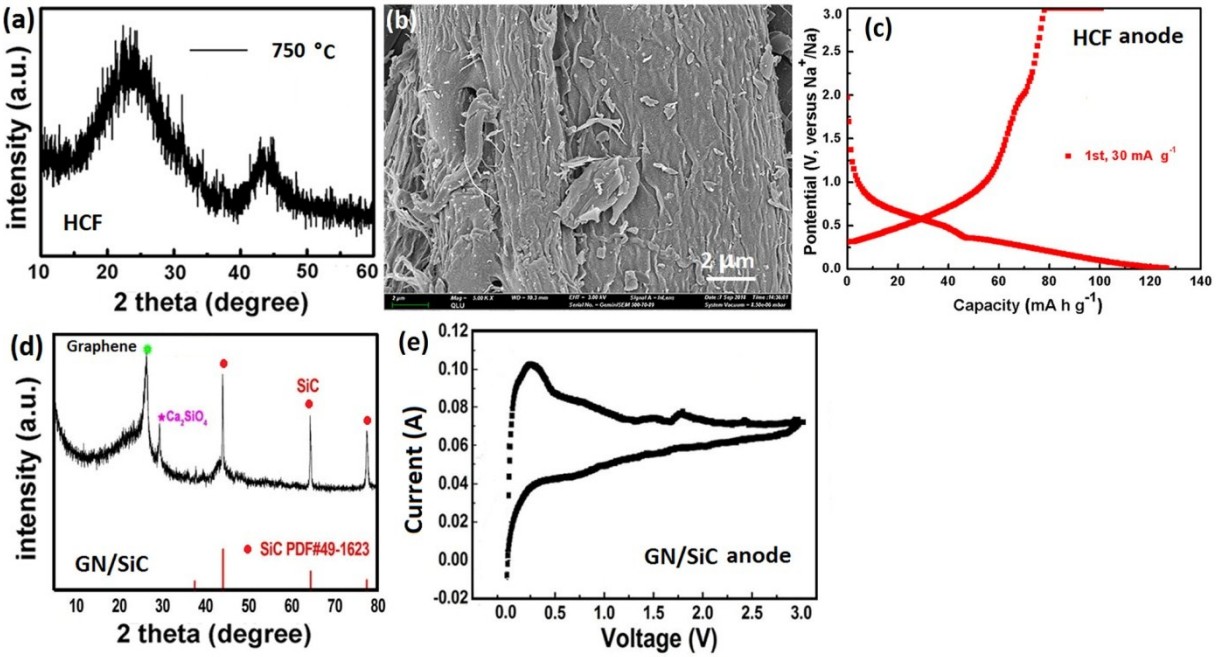

Fig. S8 (a) X-ray diffraction pattern of the hard carbon fiber (HCF) sample synthesized by pyrolysis of filter paper at 750 °C for 8 h. (b) SEM image of the HCF sample. (c) Charge/discharge profile of the HCF anode at the current density of

30 mA g^{-1}. (d) X-ray diffraction pattern of the graphene/SiC (GN/SiC) sample. (e) CV curve of the GN/SiC anode at a scan rate 0.3 mV s^{-1}.

The X-ray diffraction pattern, SEM image and the electrochemical performance of the hard carbon fiber (HCF) sample synthesized by pyrolysis of filter paper at 750 °C for 8 h are showed in Fig. S8ab, respectively. Fig. S8d shows the XRD patterns of GN/SiC sample, which is well indexed to the crystal structure of the β-SiC phase (PDF#49-1623). In addition, a broad and strong peaks at 24° appeared, corresponding to the (002) diffraction of the graphene structure. We further performed the CV test of GN/SiC electrode at a scan rate 0.3 mV s^{-1} in a potential interval of 0.01-3 V (Fig. S8e), a broad and stable peak at 0.2 V appeared, due to the formation of solid electrolyte interface (SEI) and irreversible Na insertion into the SEI. This shows that the high irreversible capacity was consumed in the formation of SEI in cycles, leading to the poor electrochemical performances of the GN/SiC anode. So we used carbonized filter paper fibers decorated with GN/SiC composite nanosheets (GN/SiC/HCF) as the flexible supporting framework to prepare a BFCF anode, and the presodiation of the BFCF anode was performed prior to cell fabrication to provide rich Na ions for its depassivation. Fig.S9a shows that the influences of binder and current collector on the electrochemical performances of different GN/SiC anodes. As shown in Fig. S9a, the PGN/SiC/HCF anode delivers reversible capacities of 501 mAh g^{-1} at the current rate of 10 mA g^{-1}, which is higher than that of the HCF anode (Fig. S8c), the GN/SiC (Al) anode with using binder and Al current collector and the GN/SiC/HCF anode without pre-sodiating. Especially, its cycling performance was greatly improved at a high current rate of 1 A g^{-1} due to the depassivation of the GN/SiC/HCF (Fig. S9b). Fig. S9c show the charge/discharge curves of the PGN/SiC/HCF anode at the different current rates. The electrode delivers reversible capacities of 501,370, 327, 276, 208 and 100 mA h g^{-1} at the current rate of 0.01, 0.1, 1, 2 , 10 and 20 A g^{-1}, respectively. Fig. S9d shows the long cycling performance of the

PGN/SiC/HCF anode at a constant current rate of 1 A g^{-1}, which shows a capacity of 234.33 mAh g^{-1} after 791 cycles with a high capacity retention of 91%, exhibiting a high coulombic efficiency.

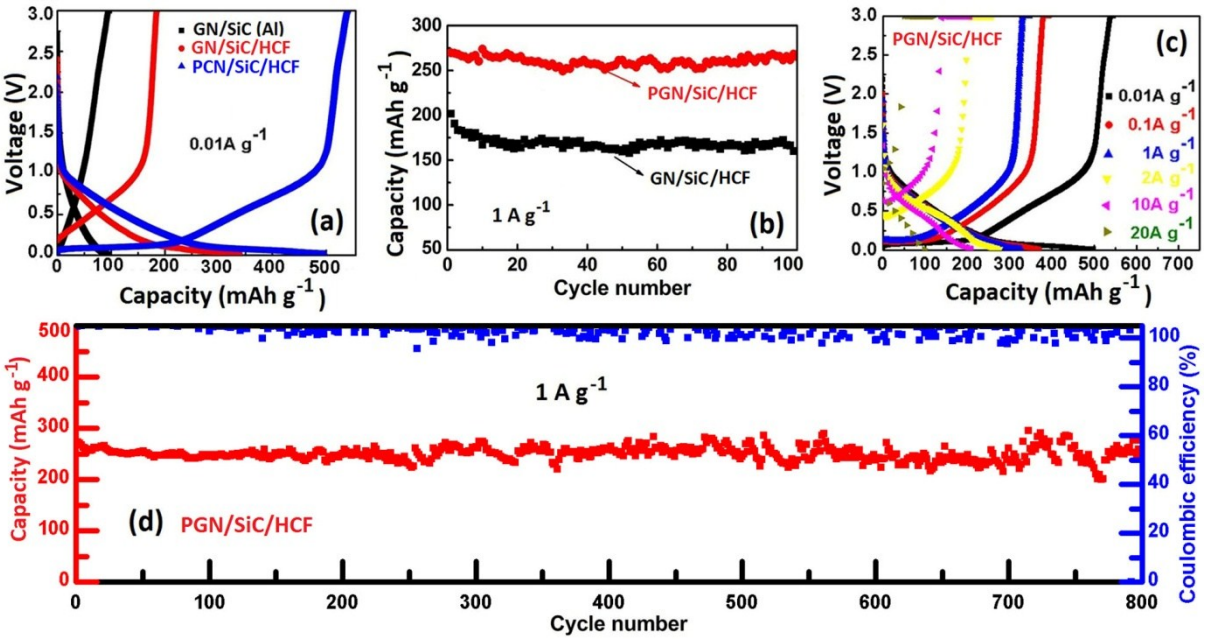

Fig. S9 The electrochemical performance characterizations of different anodes in the sodium ion half-cell (SIHC) form. a) The typical charge/discharge profiles of different anodes. b) Cycling performances of the GN/SiC/HCF and the PN/SiC/HCF anodes. c) The charge/discharge profiles of the PGN/SiC/HCF anode at different current rates. d) Cycling performance of the PGN/SiC/HCF anode at the current rate of 1A g^{-1}.

S9: Formation mechanism and characterizations of BFCF-NVP/HCF sample

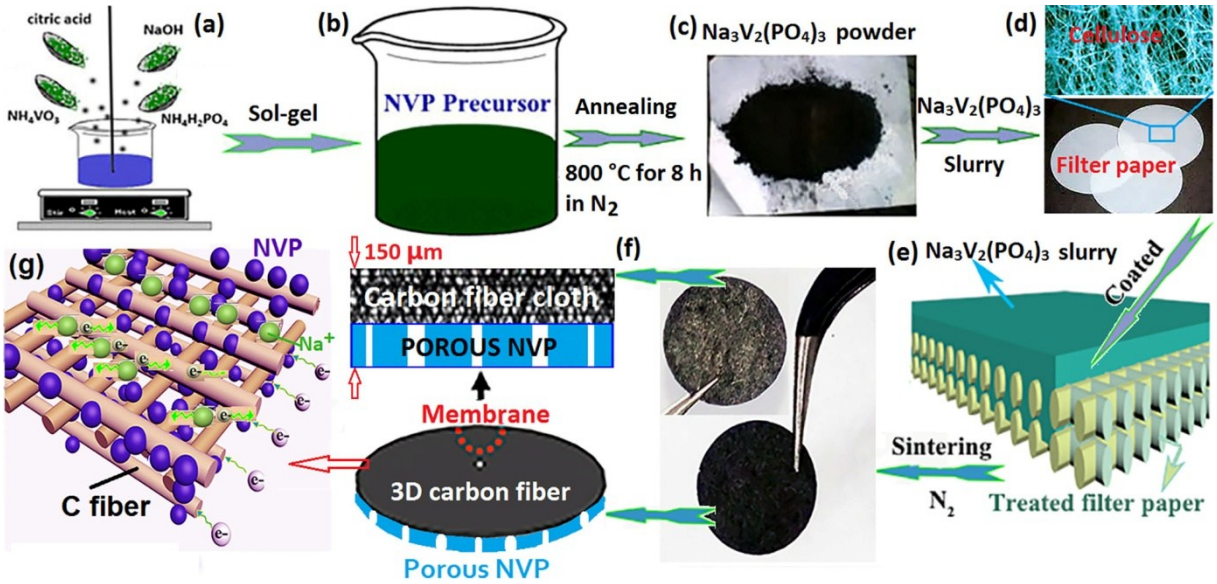

Fig. S10 Schematic illustration of the synthesis process for the BFCF-NVP/HCF cathode. a-c) the synthesis procedure of the NVP powers synthesized by a sol-gel method, d-f) the synthesis procedure of the BFCF-NVP/HCF cathode, and g) structure illustration of the BFCF-NVP/HCF cathode.

Fig. S10 schematically illustrates the preparation processes of NVP precursor and BFCF-NVP/HCF cathode. First, NVP powers were prepared by a sol-gel method (Fig. S10a-c) and dispersed in N-methylpyrrolidone (NMP) to form a slurry. Second, the slurry was coated on a filter paper spread over a glass plate, then it was dried and sintered to form theBFCF-NVP/HCF cathode (Fig. S10d-f). The structure of the BFCF-NVP/HCF cathode is shown in Fig. S10g for clarity. The unique cellulose structure of filter paper was turned into a 3D conductive network framework of HCF and porous NVP was evenly coated on the HCF framework via the synthesis. When the BFCF-NVP/HCF was used as a cathode for FSIFBs, there are several notable advantages. Firstly, the HCF increases the active constituent part, charge reaction and Na^+ storage sites of NVP, directly resulting in a significant improvement of the Na^+ transportation and the conductivity of the composite cathode. Secondly, the flexible cross-linked porous framework of HCF and the porous structure of NVP in the BFCF-NVP/HCF not only are favour of Na^+ insertion/desertion during the charging/discharging processes, but also offer an elastic buffer to accommodate the volume change of NVP, benefiting to an excellent cycle performance.

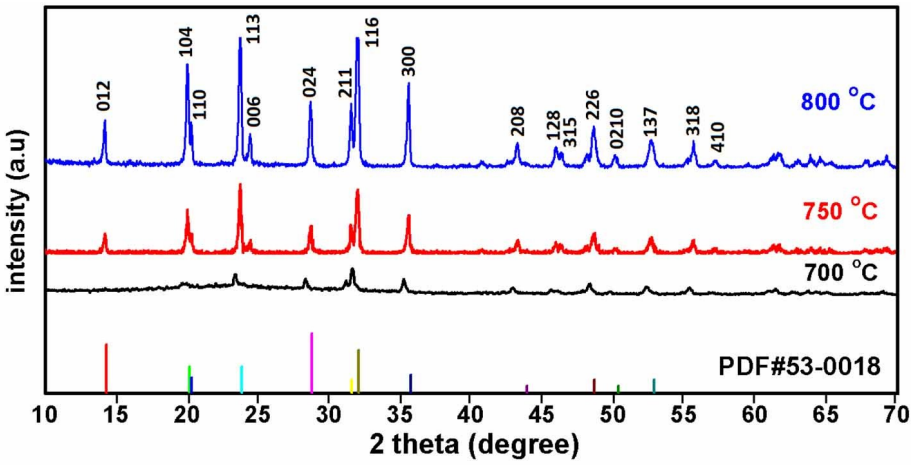

Fig. S11 XRD patterns of the BFCF-NVP/HCF samples synthesized at different temperature.

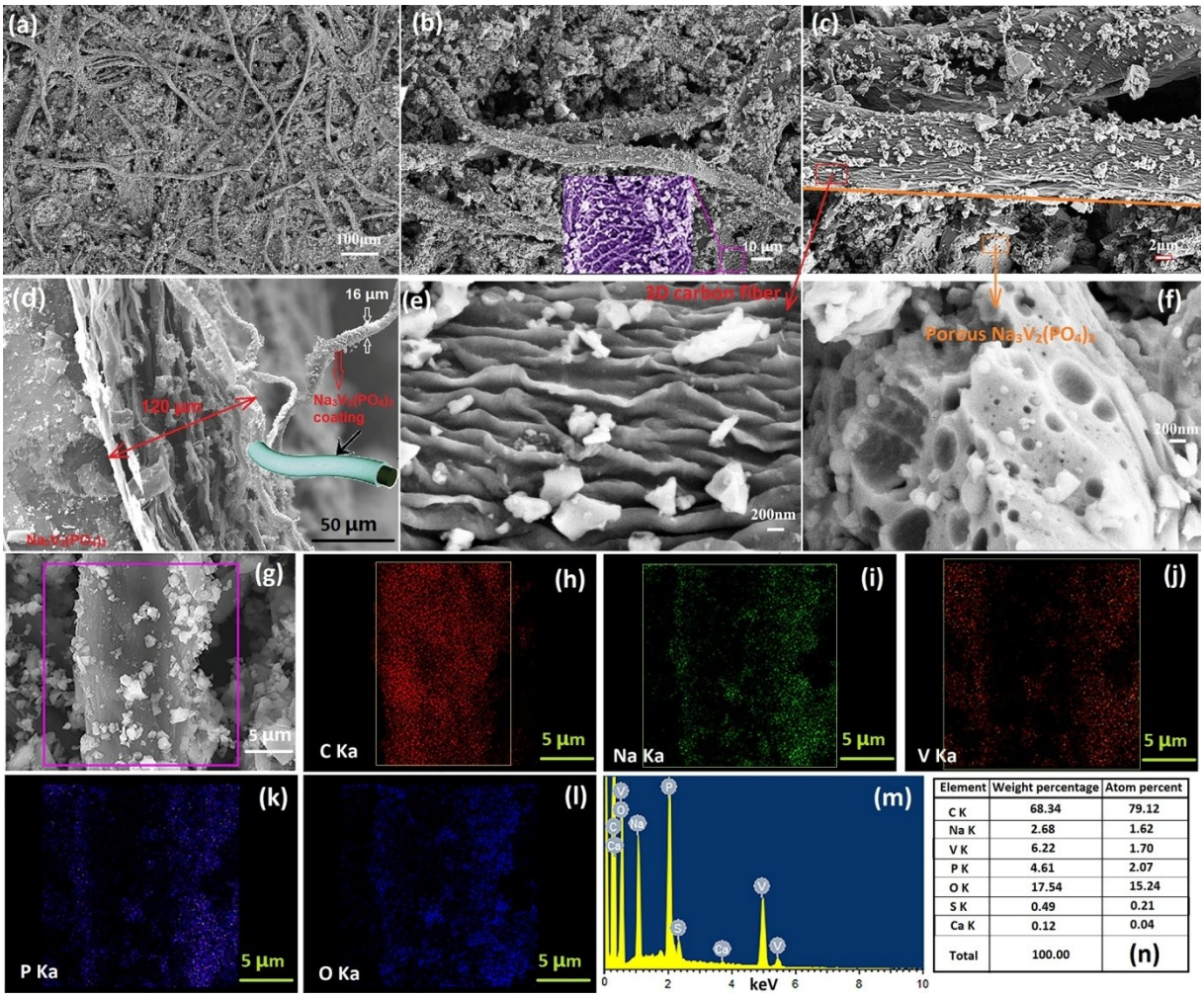

Element	Weight percentage	Atom percent
C K	68.34	79.12
Na K	2.68	1.62
V K	6.22	1.70
P K	4.61	2.07
O K	17.54	15.24
S K	0.49	0.21
Ca K	0.12	0.04
Total	100.00	

Fig. S12 Morphology characterization of the BFCF-NVP/HCF cathode synthesized at 750 °C. a-f) SEM images. g-l) SEM-EDS images. m, n) The energy spectra.

Morphology of the BFCF-NVP/HCF cathode synthesized at 750 °C was shown in Fig. S12. The SEM images in Fig. S12a,b show the top-view of the BFCF-NVP/HCF cathode, indicating that the 3DHCF formed by the high temperature carbonization of the filter paper still preserves the fiber interweaving structure and shows no obvious fracture or breakage. Fig. S12c-e show a fracture surface morphology of the BFCF-NVP/HCF, indicating that it is composed of the 3DHCF framework and PNVP with macrosporous structure of 50–300 nm (Fig. S12f). Moreover, the fold framework structure of 3DHCF (Fig. S12e) and the porous structure of PNVP facilitate the infiltration of the electrolyte. Fig. S12g-n are the SEM-EDS images and energy spectra of the BFCF-NVP/HCF, which show very clearly that the PNVP (Fig. S12i-l) was applied evenly on the surface of HCF (Fig. S12h). To determine the elemental content of the BFCF-NVP/HCF cathode, quantitative analysis was performed using energy dispersive spectrometry (EDS) (Fig. S12m and 12n). The results indicate that the atom percent of C is 79.12, and the atom percent of S is very limited (0.49) (Fig. S12n).

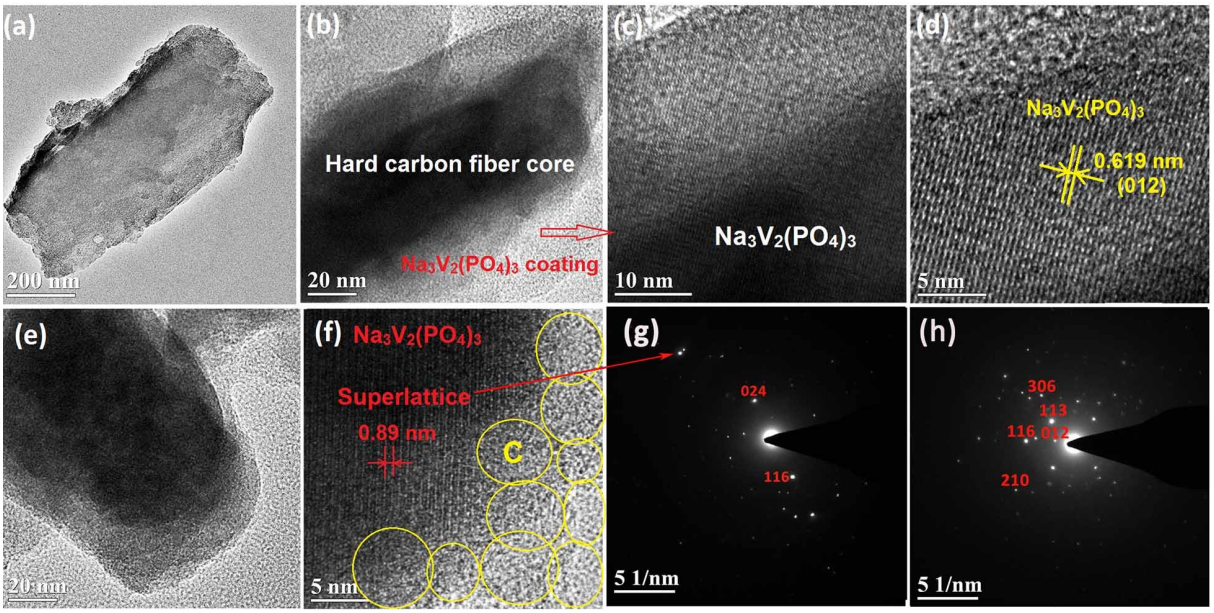

Fig. S13 Microstructural characterization of the BFCF-NVP/HCF cathode synthesized at 750 °C. a-h) HRTEM images and associated SAED patterns of the BFCF-NVP/HCF cathode.

Fig. S13 shows the high resolution transmission electron microscopy (HRTEM) images of the BFCF-NVP/HCF sample synthesized at 750 °C. Fig. S13a-e show the core diameter of single HCF is about 60 nm (Fig.S13b,e), and the thickness of NVP shell with the lattice fringe of (012) plane is about 30 nm (Fig. S13d). Moreover, the selected area electron diffraction patterns (SAED) in Fig. S13g,h show the diffraction spots belonging to NVP crystal structure, which are consistent with the results of XRD patterns (Fig. S11). The super lattice structure with the interplanar spacing of 0.89 nm in Fig. S13f is further evidenced by the diffraction spot in Fig, S13g, showing that HCF can induce the nucleation and growth of NVP crystal particle and form super lattice structure in the synthesis. The super lattice structure has abundant reactive sites of electron and Na^+ in the quantum wells due to quantum confinement and size effects.[19]

S10. Elementary analysis and the counting process of the actual mass of NVP active material in BFCF-NVP/HCF

The carbon content in BFCF-NVP/HCF and NVP/C is measured to be 49.33 and 5.755wt% (Table S5), respectively, so the amount of the HCF in BFCF-NVP/HCF is calculated to be 43.6 wt%, indicating that the mass ratio of NVP/C:HCF in the BFCF-NVP/HCF is 56.6:43.4. In this work, the total mass of BFCF-NVP/HCF is 4.5 mg, so the actual mass loading of NVP active material in BFCF-NVP/HCF is about 2.34 mg cm^{-2} . The calculation process is as follows:[18]

the actual mass of NVP active material is 4.5×56.6%×(1-0.05755)=2.39 mg.

The area of filter paper is 3.14×0.57×0.57=1.02 cm^2.

So, the actual mass loading of NVP active material in BFCF-NVP/HCF is about 2.40/1.02= 2.34 mg cm^{-2}.

Table S5 Elementary analysis results of different samples with using a Vario EL IIICHN elemental analyzer.

Sample name	Sample wight [mg]	Element content [wt%]
BFCF-NVP/HCF	2.9010	N: 0.976

		C: 49.33 S: 2.044 H: 4.997
NVP/C	6.9080	N: 0.541 C: 5.755
		S: 0.040

References

[1] W. Wang, Q. J. Xu, H. M. Liu, Y. G. Wang and Y. Y. Xia, A flexible symmetric sodium full cell constructed using the bipolar material $Na_3V_2(PO_4)_3$, J. Mater. Chem. A, **2017**, 5, 8440-8450.

[2] B. Long, J. Zhang, L. Luo, G. Ouyang, M.-S. Balogun, S. Song and Y. Tong, High pseudocapacitance boosts the performance of monolithic porous carbon cloth/closely packed TiO_2 nanodots as an anode of an all-flexible sodium-ion battery, *J. Mater. Chem. A*, accepted on 02 Jan **2019** and first published on 03 Jan 2019.

[3] W. Zhang, Y. Liu, C. Chen, Z. Li, Y. Huang and X. Hu, Flexible and Binder-Free Electrodes of Sb/rGO and $Na_3V_2(PO_4)_3$/C/rGO Nanocomposites for Sodium-Ion Batteries, *Small*, **2015**, *11*, 3822-3829.

[4] D. M. Xu, D. L. Chao, H. W. Wang, Y. S. Gong, R. Wang, B. B. He, X. L. Hu and H. J. Fan, Flexible Quasi-Solid-State Sodium-Ion Capacitors Developed Using 2D Metal-Organic-Framework Array as Reactor *Adv. Energy Mater.* **2018**, 8, 1702769.

[5] N. Li, Z. P. Chen, W. C. Ren, F. Li and H. M. Cheng, Flexible graphene-based lithium ion batteries with ultrafast charge and discharge rates, PNAS. **2012,** 109, 17360-17365.

[6] P. Xiong, L. L. Peng, D. H. Chen, Y. Zhao, X. Wang and G. H. Yua, Two-dimensional nanosheets based Li-ion full batteries with high rate capability and flexibility, *Nano Energy* **2015**, *12*, 816-823.

[7] X. F. Wang, B. Liu, X. J. Hou, Q. F. Wang, W. W. Li, D. Chen and G. Z. Shen, Ultralong-life and high-rate web-like $Li_4Ti_5O_{12}$ anode for high-performance flexible lithium-ion batteries, *Nano Research* **2014,** *7*, 1073–1082.

[8] G. Zhou, Y.-E Miao, Z. Wei, L. Mo, F., Y. Wu, J. Ma and T. Liu, Bioinspired Micro/Nanofluidic Ion Transport Channelsfor Organic Cathodes in High-Rate and Ultrastable Lithium/Sodium-Ion Batteries, *Adv. Funct. Mater.* **2018,** 1804629.

[9] W. Ren, X. Yao, C. Niu, Z. Zheng, K. Zhao, Q. An, Q. Wei, M. Yan, L. Zhang and L. Mai, Cathodic polarization suppressed sodium-ion full cell with a 3.3 V high-voltage, *Nano Energy*, **2016**, *28*, 216.

[10] S. Yuan, Y.-H. Zhu, W. Li, S. Wang, D. Xu, L. Li, Y. Zhang and X.-B. Zhang, Surfactant-Free Aqueous Synthesis of Pure SingleCrystalline SnSe Nanosheet Clusters as Anode for High Energy- and Power-Density Sodium-Ion Batteries，*Adv. Mater.* **2016**, DOI: 10.1002/adma.201602469.

[11] M. Sheng, F. Zhang, B. Ji, X. Tong, Y. Tang, A Novel Tin-Graphite Dual-ion battery Based on Sodium-Ion Electrolyte with High Energy Density, *Adv.Energy Mater.* **2017**, *7*, 1601963.

[12] S. Chen, F. Wu, L. Shen, Y. Huang, S. K Sinha, V Srot, P. A. van Aken, J. Maier and Y. Yu, Cross-Linking Hollow Carbon Sheet Encapsulated CuP_2 Nanocomposites for High Energy Density Sodium-Ion Batteries, *ACS Nano*, **2018**, *12* (7), 7018–7027.

[13] J. Deng, W.-B. Luo, X. Lu, Q. Yao, Z. Wang, H.-K. Liu, H. Zhou, S.-X. Dou, High Energy Density Sodium-Ion

Battery with Industrially Feasible and Air-Stable O_3-Type Layered Oxide Cathode, *Adv.Energy Mater.* **2018**, *8*, 1701610.

[14] J. Zhao, G. Wang, R. Hu, K. Zhu, K.Cheng, K. Ye, D. Cao and Z. Fan, Ultrasmall-sized SnS nanosheets vertically aligned on carbon microtubes for sodium-ion capacitors with high energy density, *J. Mater. Chem. A*, **2019**,*7*, 4047-4054.

[15] P. Xue, N. Wang, Z. Fang, Z. Lu, X. Xu, L. Wang, Y. Du, X. Ren, Z. Bai, S. Dou and G.Yu, Rayleigh-Instability-Induced Bismuth Nanorod@Nitrogen-Doped Carbon Nanotubes as A Long Cycling and High Rate Anode for Sodium-Ion Batteries, *Nano Lett.*, **2019**, DOI:10.1021/acs.nanolett.8b05189.

[16] L.L. Zhang, H.B. Sun, X.L. Yang, Y.W. Wen, Y.H. Huang, M. Li, G. Peng, H.C. Tao, S.B. Ni and G. Liang, *Electrochim. Acta* **2015**, 152, 496–504.

[17] Y. Xu, Q. Wei, C. Xu, Q. Li, Q. An, P. Zhang, J. Sheng, L. Zhou and L.Mai, *Adv. Energy Mater.* **2016**, 6, 1600389.

[18] Y.S. Chen, D. Zhang, X.F. Bian, X.F. Bie, C.Z. Wang, F. Du, M. Jang, G. Chen and Y.J. Wei, *Electrochim. Acta*, **2012,** 79, 95–101.

[19] L.L. Zhang, Z. Li, X.L. Yang, X.K. Ding, Y.X. Zhou, H.B. Sun, H.C. Tao, L.Y. Xiong and Y.H. Huang, *Nano Energy*. **2017**, 34, 111–119.